Impact of the lanthanide size on the polymorphism and electrical properties of $Ln_{5.4}MoO_{11.1}$ (Ln = Nd, Sm and Gd)

Rafael Rubio-Vives[1], José M. Porras-Vázquez[1,*], Lucía dos Santos-Gómez[1], Javier Zamudio-García[1], Antonia Infantes-Molina[1], Jesús Canales-Vazquez[2], David Marrero-López[3], Enrique R. Losilla[1]

1 Universidad de Málaga, Dpto. de Química Inorgánica, Cristalografía y Mineralogía 29071-Málaga, Spain

2 Renewable Energy Research Institute, Escuela Técnica Superior de Ingenieros Industriales de Albacete, University of Castilla-La Mancha, 02071-Albacete, Spain

3 Universidad de Málaga, Dpto. de Física Aplicada I, 29071-Málaga, Spain

KEYWORDS: hydrogen separation membrane, lanthanide molybdate, polymorphism, mixed ionic-electronic conductor

ABSTRACT:

Mixed proton-electronic conductors are of great interest for high temperature electrochemical devices, such as hydrogen separation membranes. In this contribution, ceramics with composition $Ln_{5.4}MoO_{11.1}$ (Ln = Nd, Sm and Gd) were prepared by a freeze-drying precursor method. The resulting powders were sintered at 1500 ºC and cooled down at different rates to investigate the different polymorphic forms: quenching (rapid cooling), 5 and 0.5 ºC min^{-1}. The ceramics were characterized by different techniques: X-ray diffraction, scanning and transmission electron microscopies and X-ray photoelectron and impedance spectroscopies. X-ray diffraction studies confirmed that all materials are single phase regardless of the cooling rate used. Those cooled by quenching present a simple cubic fluorite structure. At lower rates, 5 and 0.5 ºC min^{-1}, the cubic symmetry is stabilized as the size of the lanthanide decreases. However, electron diffraction studies indicated the formation of domains with superstructure ordering. Furthermore, XPS analysis showed the presence of mixed Mo^{6+} and Mo^{5+} for all compositions, which explains the electronic conduction in an oxidizing atmosphere. All materials are stable in reducing atmosphere and the ionic and electronic conductivities show opposite trends as the ionic radii of the lanthanide element becomes smaller, where the former decreases and the latter increases.

1. Introduction

Nowadays, hydrogen is one the most promising energy vectors due to its high gravimetric energy density energy and clean reaction product, H_2O.[1-3] It can be obtained through water-splitting,[4,5] a still expensive technology, or via the reforming of hydrocarbons,[6,7] more economically viable. However, this procedure results in the generation of other by-products, such as CO and CO_2, and minor impurities such as SO_x, NO_x and VOCs (Volatile Organic Compounds), which need to be separated from H_2. This process can be performed by a ceramic hydrogen separation membrane, electrochemical devices where H_2 molecules split into H^+ and e^- on the feed side of the membrane and recombine at the other side to generate a high purity H_2 flux.[8,9] Therefore, candidates for hydrogen separation membranes must possess a high proton and electronic conductivity, as well as chemical stability under operation conditions.

Materials based on perovskites, such as doped $BaCeO_{3-\delta}$ and $BaZrO_{3-\delta}$, are the most widely investigated candidates for hydrogen separation membranes due to their high proton conductivity at intermediate temperatures (500-800 ºC).[10,11] However, they present serious stability issues in the presence of CO_2, a gas present after hydrocarbon reforming.[12,13] Alternative candidates based on lanthanum tungstates ($La_{6-x}WO_{12-\delta}$) have been investigated in the last years, which exhibit a good proton conductivity and improved stability in the presence of a CO_2-rich atmosphere.[14-16] In addition, the mixed proton-electronic conductivity of these materials can be enhanced by the substitution of W^{6+} by Mo^{6+}, due to the higher reducibility of the latter.[17-19]

In the last years, our research group has studied the influence of the synthesis-sintering conditions on the structural and electrical properties of the $La_{6-x}MoO_{12-\delta}$ ($0 \leq x \leq 3.0$) series.[20,21] Precursor powders of these materials were prepared by the freeze-drying method, calcined at 1500 ºC and then cooled down at different rates: rapid cooling from 1500 ºC by quenching, 5 and 0.5 ºC min^{-1}. Those samples cooled down by quenching, regardless of the lanthanum content, crystallized with a cubic fluorite symmetry. A different behaviour was observed by cooling at 5 ºC min^{-1}, where samples with a (7 × 7 × 1) rhombohedral superstructure, relative to a single cubic fluorite, were obtained for lanthanum contents of $0 \leq x \leq 1$, denominated in this work as R1. For lower lanthanum contents, $x \geq 1.5$, a cubic related fluorite-type structure is stabilized. A different rhombohedral polymorph with a 5 × 5 × 1 superstructure, denoted in this work as R2, is obtained at a cooling rate of 0.5 ºC min^{-1} for high lanthanum contents ($x \leq 1$). Lower lanthanum contents, $x \geq 1.5$, results in the formation of a monoclinic phase, originally reported by Dan Vu *et al.*[22] In a very recent work, the structure of R1 and R2 polymorphs was determined by a combination of select area electron diffraction data and De Wolff´s theory.[23] The obtained models were satisfactorily applied in the Rietveld refinement of neutron powder diffraction data.[21] In terms of electrical properties, the highest overall conductivity values were found for the cubic quenched phases due to their higher symmetry. However, opposite trends were observed for the ionic and electronic conductivities along the $La_{6-x}MoO_{12-\delta}$ ($0 \leq x \leq 3.0$) series. The ionic conductivity slightly decreases with a smaller La content, from 0.17 mS cm^{-1} for $La_{5.4}MoO_{11.1}$ to 0.14 mS cm^{-1} for La_4MoO_9, at 700 ºC in a dry N_2 atmosphere. On the other hand, the electronic conductivity increases with a smaller La content, from 5.0 mS cm^{-1} for $La_{5.4}MoO_{11.1}$ to 9.5 mS cm^{-1} for La_4MoO_9, at 700 ºC in a wet 5% H_2-Ar atmosphere.

Apart from lanthanum molybdates, other lanthanides have been also explored by Shlyakhtina´s group with general formula $Ln_{6-x}MoO_{12-\delta}$ (Ln = Nd, Sm, Gd, Dy, Ho, Er, Tm, Yb, Lu; x = 0 and 0.5).[24,25] At 1600 ºC, middle size lanthanide molybdates (Nd-Dy) crystallise with a cubic fluorite structure (s.g. F m-3m), whereas the smaller ones (Ho-Lu) present a cubic bixbyitetype structure (s.g. I a -3). However, in these works the influence of the cooling rate on the final crystal structure symmetry of the sample was not examined. In terms of electrical properties, it was observed that the proton conductivity decreases as the size of the lanthanide becomes smaller.

The aim of this work is to carry out a thorough study of the influence of the lanthanide-type and synthesis-sintering conditions on the polymorphism and electrical properties of lanthanide molybdates with general formula, $Ln_{5.4}MoO_{11.1}$ (Ln = Nd, Sm and Gd). The structural and microstructural features of these materials were studied by X-ray powder diffraction (XRPD), X-ray photoelectron spectroscopy (XPS) and transmission and scanning electron microscopy (TEM and SEM). The electrical characterization was carried out by impedance spectroscopy under different flowing atmospheres.

2. Experimental

2.1. Synthesis

Samples with composition $Ln_{5.4}MoO_{11.1}$ (Ln = Nd, Sm and Gd) were prepared by a freeze-drying precursor method, following the synthetic procedure described in detail in a previous report for $La_{5.4}MoO_{11.1}$.[20] The starting reagents were Ln_2O_3 (Ln = Nd, Sm and Gd, 99.99%, Sigma-Aldrich) and MoO_3 (99.5%, Sigma-Aldrich). The precursor solutions were prepared by dissolving separately Ln_2O_3 and MoO_3 in diluted nitric acid and diluted ammonia, respectively. An ethylenediaminetetraacetic acid solution (EDTA 99.99%, Sigma-Aldrich), dissolved in ammonia, was added as a chelating agent in a 1:1 metal to EDTA ratio. The different cation solutions were mixed in stoichiometric amounts under stirring, obtaining transparent solutions with a concentration of approximately 0.1 mol L^{-1} and pH = 7. The solutions were frozen into liquid nitrogen and then dehydrated by vacuum sublimation in a Scanvac-Coolsafe freeze-dryer for 2 days. The dried precursor powders were firstly calcined at 300 ºC to partially decompose the dried solid precursors and then at 800 ºC for 1 h to remove the remaining carbonaceous species. The resulting powders were compacted into pellets with size of 10 and 1 mm of diameter and thickness, respectively; and sintered at 1500 ºC for 1 h with a heating rate of 10 ºC min^{-1} and finally cooled down at three different rates: quenching (rapid cooling), 5 and 0.5 ºC min^{-1}. The obtained pellets were finely ground into powder for structural characterisation. Hereafter, all samples are labelled as Ln$_{5.4}$C, where Ln is the lanthanide and C is the cooling rate.

2.2. Structural and microstructural characterisation

The purity of all samples was analysed by laboratory X-ray powder diffraction (XRPD) using a PANalytical Empyrean diffractometer with CuK$\alpha_{1,2}$ radiation. Phase identification was performed with the X'Pert HighScore Plus software.[26] For the structural analysis, data were collected with a X’Pert Pro MPD (PANalytical) automated diffractometer equipped with a Ge(1 1 1) primary monochromator (CuKα_1 radiation) and an X’Celerator detector over the 2θ angular range of 10-110º with an acquisition time of 4 h. The structural analysis was carried out with the GSAS software.[27]

The crystal structure of the materials was also investigated by selected area electron diffraction (SAED) and high-resolution transmission electron microscopy (HRTEM). Specimen observation was performed on a Jeol JEM 2100 electron microscope operating at 200 kV equipped with a ±25° double-tilt sample holder. TEM images were analysed using the Digital Micrograph™ software from Gatan.[28]

X-ray photoelectron spectroscopy (XPS) measurements were recorded on a Scienta ESCA 200 Spectrometer operating with a monochromatic X-ray source Al(Kα) of photons at 1486.6 eV under an ultra-high vacuum of 10^{-10} mbar. The experimental methodology of XPS contained 0.65 eV Au $4f_{7/2}$ line of full width at half maximum. A Multipak-V9.3 software package was used for data analysis. A Shirley-type background was subtracted from the signals, and the recorded spectra were always fitted using Gaussian−Lorentzian curves in order to determine more accurately the binding energy of the different element core levels.[20] The XPS spectra were collected on as-prepared and reduced samples (annealed at 800 ºC for 24 h in a flowing 5% H_2-Ar atmosphere) in order to evaluate the possible reduction of the cations in very reducing conditions.

The morphology and cation composition of the electrodes were investigated by field emission scanning electron microscopy (FEI-SEM, Helios Nanolab 650), combined with energy dispersive spectroscopy (EDS, Oxford Instruments). The grain size of the dense pellets was estimated from the SEM micrographs, using the linear intercept method.[29]

2.3. Electrical characterisation

The electrical conductivity was determined by impedance spectroscopy using a frequency response analyser (Solartron 1260 FRA) in dry and wet (2 vol.% H_2O) N_2 and wet 5% H_2-Ar flowing gases. The data were collected in the 0.01 Hz to 1 MHz frequency range with an ac perturbation of 50 mV on cooling from 750 to 100 °C and a dwell time of 30 min at each measurement temperature. Pt current collectors were formed by coating the pellet surfaces with Pt-ink (METALOR® 6082) and then firing at 800 ºC for 1 h in air. The data were analysed by using the ZView program.[30] The conductivity was also determined as a function of the oxygen partial pressure to evaluate the different ionic and electronic contributions to the total conductivity. The pellet samples were reduced in 5% H_2-Ar for 12 h at 700 ºC in a closed tube furnace and the conductivity was continuously measured by the Van der Pauw method. The oxygen partial pressure was monitored with an YSZ oxygen sensor during the slow reoxidation process.

3. Results and discussion

3.1. Single phase existence range

XRPD patterns of the $Ln_{5.4}MoO_{11.1}$ (Ln = Nd, Sm and Gd) precursors heated at 800 ºC for 1 h are shown in Figure S1. All samples present broad diffraction peaks, due to the nanocrystalline nature of the as-synthesised materials, with an average crystallite size of 12 nm diameter (determined with the Scherrer equation). All patterns can be indexed as a single cubic fluorite with cell parameters of 5.568(1), 5.475(1) and 5.425(1) Å for Nd, Sm and Gd samples, respectively, following the expected trend considering the ionic radii of the rare-earth elements (1.109, 1.079 and 1.053 Å for Nd^{3+}, Sm^{3+} and Gd^{3+}, respectively, in an 8-fold coordination). A different behaviour is observed when the samples are sintered at 1500 ºC and cooled down to room temperature at different rates. As can be observed in Fig. 1, different polymorphic phases are stabilised depending on the composition and cooling rate. No secondary phases are detected for any of the samples and Table 1 summarises the different polymorphs obtained for all compositions and cooling rates.

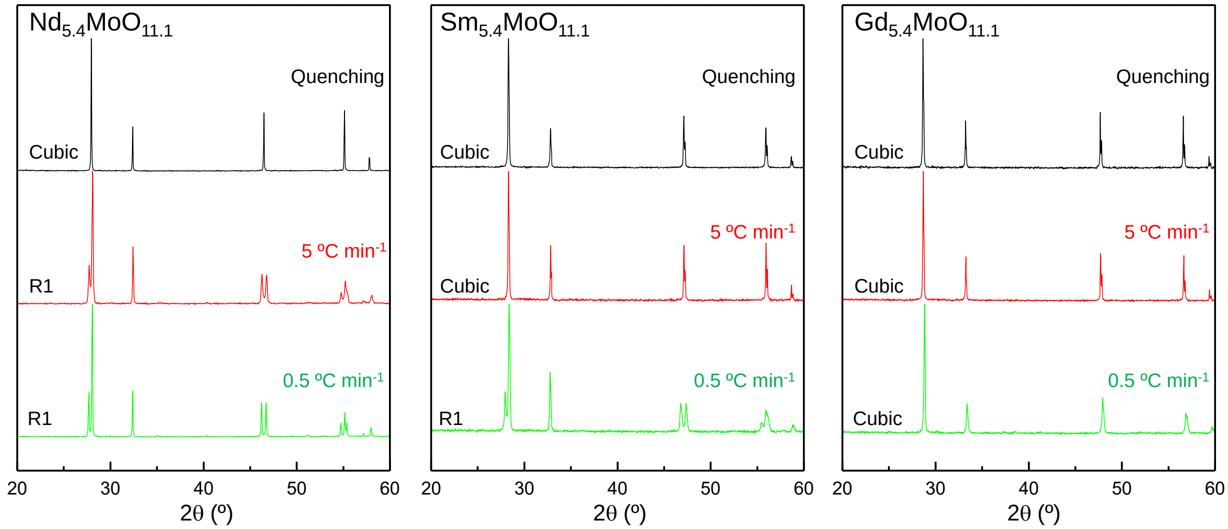

Figure 1. XRPD patterns of $Ln_{5.4}MoO_{11.1}$ (Ln = Nd, Sm and Gd) heated at 1500 ºC for 1h and cooled down by quenching, 5 and 0.5 ºC min^{-1}. The symmetry for each sample is denoted at the bottom left of the diffraction patterns.

All quenched samples crystallise as a cubic fluorite, similar to $La_{6-x}MoO_{11.1}$ (x = 0.6 - 3)[20,21] and $La_{5.4}Mo_{1-x}Nb_xO_{11.1-x/2}$ (x = 0 - 0.2) series,[31] prepared under the same synthetic conditions. This behaviour is associated to the high thermal vibration of the lanthanide cations and molybdenum at 1500 ºC, occupying the same crystallographic position and leading to samples with the highest symmetry. Recent thermal neutron powder diffraction studies for related compositions, $La_{5.5}MoO_{11.25}$ and Nd_6MoO_{12}, confirmed this ordered-disordered phase transition on heating, where both samples transform from a rhombohedral to a cubic symmetry at ~1270 and 1140 ºC, respectively.[32,33]

At cooling rates of 5 and 0.5 ºC min^{-1}, a different behaviour is observed. $Nd_{5.4}MoO_{11.1}$ presents a rhombohedral R1 symmetry in both conditions. Shlyakhtina *et al.* have studied related compositions.[34] For instance, $Nd_{5.4}Zr_{0.6}MoO_{12.3}$ prepared at 1400 ºC for 3 h was a mixture of two cubic fluorites, although a single cubic phase was obtained after sintering at 1600 ºC. Nd_6MoO_{12} sintered at the same temperature presented a rhombohedral symmetry, similar to that obtained herein.[33]

In the present work, $Sm_{5.4}MoO_{11.1}$ crystallizes as a cubic fluorite when cooled down at 5 ºC min^{-1} but exhibits a rhombohedral symmetry at 0.5 ºC min^{-1}. Related compositions reported in the literature crystallise with a cubic fluorite, $Sm_{5.4}Zr_{0.6}MoO_{12.3}$, or a rhombohedral symmetry, Sm_6MoO_{12} and $Sm_{5.5}MoO_{11.25}$,[25] all of them sintered at 1600 ºC for 3 h. Finally, $Gd_{5.4}MoO_{11.1}$ always presents a cubic symmetry, regardless of the cooling rate, similar to $Gd_{5.5}MoO_{11.1}$ prepared at 1600 ºC for 3 h.[24]

These results suggest that the polymorphism of $Ln_{5.4}MoO_{11.1}$ (Ln = Nd, Sm and Gd) is highly dependent on the cooling rate and lanthanide size. In particular, lower cooling rates favour the stabilisation of a rhombohedral symmetry because of the higher time provided to accommodate the cations in the lattice, reaching the system the most thermodynamically stable phase. In contrast, the cubic phase is stabilized at room temperature by the sudden cooling of the quenching process. In addition, as the rare-earth cation size decreases the cubic symmetry becomes predominant, even at low cooling rates, due to a smaller difference in size between the rare-earth and Mo^{6+} (1.02 Å). This causes a lesser mismatch between the two cubic coordination spheres, leading to a higher symmetry.

3.2. Structural analysis by X-ray powder diffraction and transmission electron microscopy.

All samples were analysed by the Rietveld method using two different structural models: i) a simple cubic fluorite, and ii) a simple rhombohedral fluorite. It must be mentioned that the structural models reported for the R1 and R2 polymorphs by NPD in a previous work were not used in the present study for samples with a rhombohedral symmetry.[20] XRPD data present low intensity peaks for the superstructure reflections compared to the NPD patterns, and the structural models cannot be satisfactorily applied.

Occupancy factors were modified to reflect the compositions and theoretical stoichiometries where, for both structural models, the cations (Nd, Sm, Gd and Mo) are located in the same crystallographic positions, with their isotropic displacement parameters constrained to the same value. Parameters such as unit cell, scale factor, background, and peak shape coefficients and isotropic displacement parameters were refined. Figure 2 and Table 1 show that the refinements are quite good with very low disagreement factors, with values in the range of 2-5 and 2-3 % for R_{wp} and R_F, respectively.

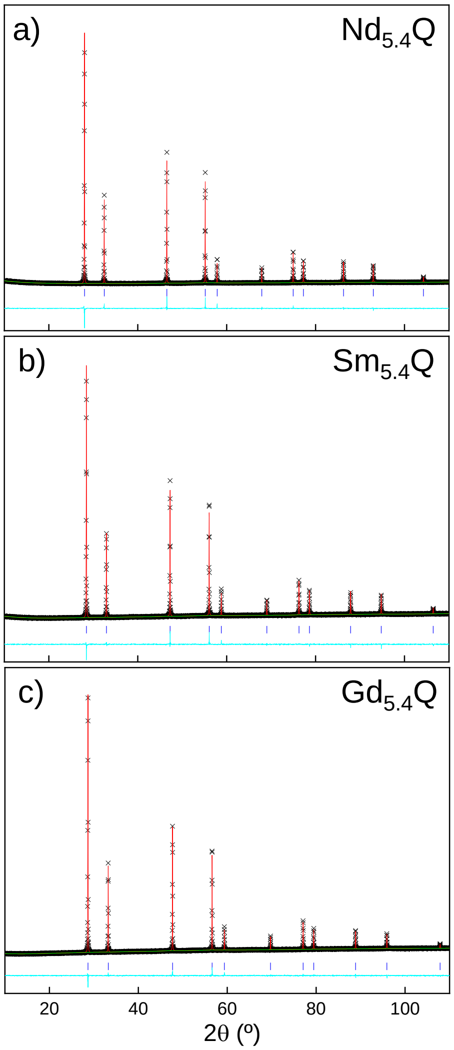

Figure 2. Rietveld plots for (a) $Nd_{5.4}Q$, (b) $Sm_{5.4}Q$ and (c) $Gd_{5.4}Q$. [Observed data (×), calculated pattern (red line), and difference curve (cyan line)]. Blue symbols mark the reflections.

Unit cell volumes, for any cooling rate, show a clear decrease as the lanthanide becomes smaller (Table 1). For instance, the quenched samples present cell volumes of 42.12(1), 40.29(1) and 39.19(1) for $Nd_{5.4}Q$, $Sm_{5.4}Q$ and $Gd_{5.4}Q$, respectively. On the other hand, only slight variations in the cell volumes are detected for samples with the same composition but different cooling rates, likely due to small variations in the oxygen content.

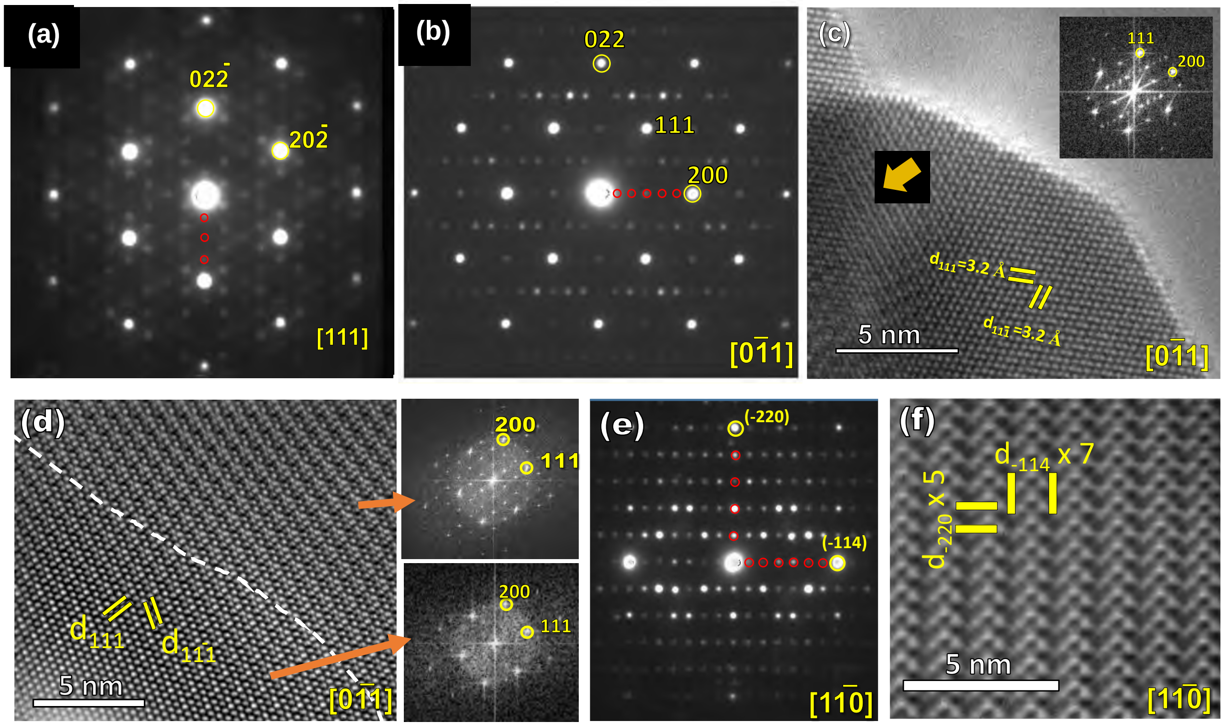

Figure 3. (a-b) SAED image in the [111] and [011] zone axis of $Sm_{5.4}5$, showing a 4×4 superstructure relative to a basic cubic fluorite; (c) HRTEM image of $Sm_{5.4}5$ in the [011] zone axis with the presence of crystalline domains with different atomic ordering. (d) HRTEM of $Nd_{5.4}0.5$ showing crystalline domains without and with superstructure ordering, which are confirmed by FFT image. (e) SAED image in the [1-10] zone axis of $Nd_{5.4}0.5$ showing a 5×7 superstructure along different crystallographic directions, and (f) the corresponding HRTEM image.

The local crystal structure, analysed by combined SAED and HRTEM, reveal the presence of crystalline nanodomains with different superstructure ordering. For instance, $Sm_{5.4}5$, which is considered as a single cubic fluorite by conventional XRPD, shows additional reflections in several crystal and SAED images. In the [111] zone axis, the most intense reflections correspond to a single cubic fluorite but the presence of weak diffuse reflections along the main crystallographic directions suggests the formation of a 4 × 4 superstructure relative to a basic cubic fluorite with a cell parameter of 5.2 Å (Figure 3a). The same behaviour is observed in the [0-11] zone axis (Figure 3b) and the corresponding HRTEM image shows the coexistence of crystalline domains without and with superstructure ordering (Figure 3c). These results suggest that $Sm_{5.4}5$ is formed by crystalline domains of cubic and R2 polymorphs, despite the average crystal structure can be considered as a cubic fluorite by XRPD. This coexistence of domains with different symmetries was already reported in a previous work for a related composition, $La_{4.5}5$, where HRTEM studies also revealed the presence of cubic and R1 domains [21]. Moreover, a similar behaviour was observed for highly doped La-CeO_2, where domains of single fluorite and C-type superstructure coexist in a same crystal.[35] In the case of $Gd_{5.4}0.5$, the SAEDs in the [111] zone axis the formation of a 4 × 4 superstructure is also observed (Figure S2).

$Nd_{5.4}0.5$ also shows crystalline domains without and with superstructure ordering (Figure 3d). The SAED in the [1-10] zone axis presents intense reflections that can be indexed in a basic rhombohedral cell (a = 3.89 Å, c = 9.66 Å) (Figure 3e); however, the weak reflections between the most intense ones suggest that the real unit cell is a 5 × 7 superstructure relative to the basic unit cell, thus an intermediate phase between the R1 and R2 polymorphs. HRTEM analysis further confirms these results (Figure 3f). This a clear evidence the complexity of these compounds, where the composition, synthesis and thermal treatment lead to the stabilization of different polymorphic phases: cubic fluorite and, 7 × 7, 5 × 5 and 4 × 4 superstructures relative to a single fluorite.

3.3. Stability in reducing conditions

In order to evaluate the suitability of these materials as hydrogen separation membranes, their stability was tested in very reducing conditions. The samples were annealed at 800 ºC for 24 h in a 5% H_2-Ar atmosphere and analysed afterwards by XRPD. Figure S3 shows the XRPD patterns of the samples after the reduction and no secondary phases are detected for any composition, retaining the original structure of the as-prepared materials. Analysis by the Rietveld method of the annealed samples led to almost identical cell parameters values respect to the as-prepared materials, as can be seen in Table S1, indicating no significant change in the oxidation states of the cations.

3.4. XPS analysis

In order to obtain information about the oxidation states of the elements on the surface, XPS analyses were performed for both as-prepared quenched samples and after their reduction at 800 ºC for 24 h in a 5% H_2-Ar atmosphere.

The O 1*s* signal corresponding to the as-prepared quenched samples evidenced, in all cases, the presence of three contributions located at ca. 528.8, 530.8 and 532.4 eV (Figure 4). The main contribution denoted as O_I (~530.8 eV) is assigned to both MoO_3 and lanthanum oxides,[36] and therefore could be related to a lanthanide molybdenum mixed oxide. The second contribution, O_{II} (~528.5 eV) is correlated to a Mo 3$d_{5/2}$ contribution and might be related to a rhombohedral polymorph, in agreement with the results obtained in the TEM section, where the analysis of the local structure indicated the presence of domains with difference symmetry. Finally, the band at 532.1 eV (O_{III}) is assigned to adsorbed oxygen or OH groups due to water uptake.[20] After reduction, this component disappears in the case of the Nd sample, reduces for Sm and hardly changes for Gd.

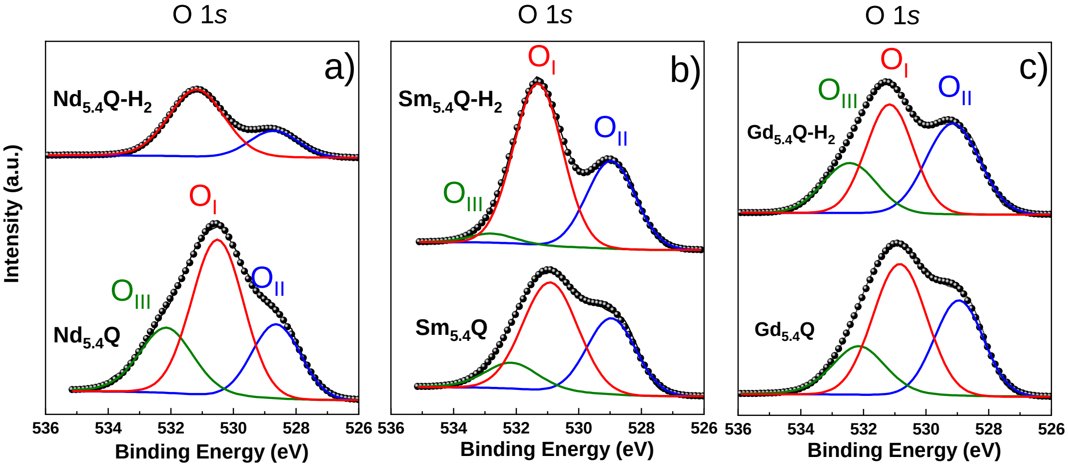

Figure 4. XPS spectra of O 1*s* core level signal for as prepared (bottom) and reduced (top) at 800 ºC for 24 h in 5%H_2-Ar for: a) $Nd_{5.4}Q$, b) $Sm_{5.4}Q$ and c) $Gd_{5.4}Q$ samples.

Regarding the Mo 3*d* core level spectra, for $Nd_{5.4}Q$ the Mo 3*d* signal overlaps with the Nd $4p_{3/2}$ signal (Figure 5a); and therefore, a proper analysis cannot be performed. In any case, the main Mo $3d_{5/2}$ contribution located at 232.3 eV is present due to the presence of the Mo^{6+} species but it is not possible to distinguish the presence of Mo^{5+} or Mo^{4+} species.

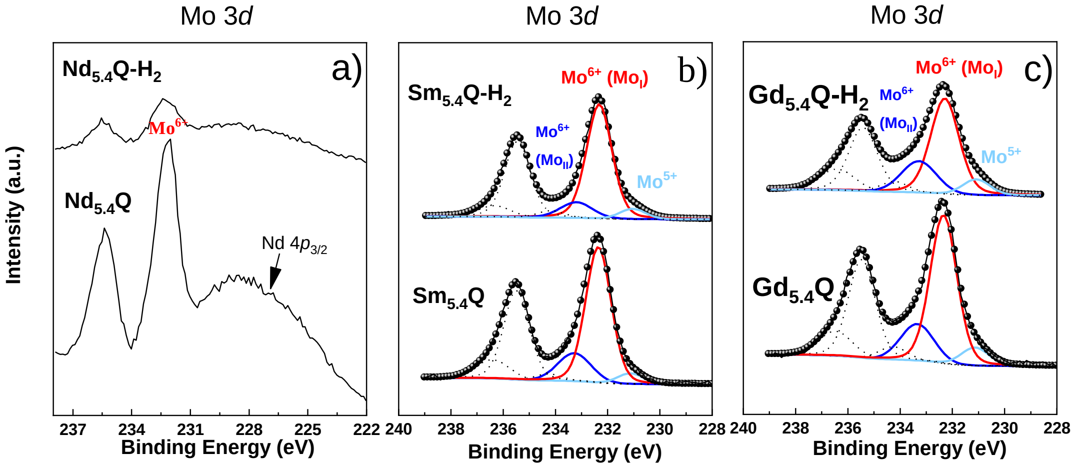

Figure 5. XPS spectra of Mo 3*d* core level signal for as prepared (bottom) and reduced (top) at 800 ºC for 24 h in 5%H_2-Ar for: a) $Nd_{5.4}Q$, b) $Sm_{5.4}Q$ and c) $Gd_{5.4}Q$ samples.

Considering the as-prepared Sm and Gd samples, the Mo 3*d* core level spectra consist of three doublets, Mo $3d_{5/2}$ and Mo $3d_{3/2}$ components, separated by 3.16 eV, with similar FWHM and area ratio Mo $3d_{5/2}$/Mo $3d_{3/2}$ = 1.5 (Figure 5bc). In order to identify the molybdenum oxidation states the Mo $3d_{5/2}$ contribution is considered. The first contribution located at 230.2 eV is due to Mo^{5+};[36] the second and most important one at ~232.1 eV refers to Mo^{6+} species and is denoted as Mo_I since it is related to the O_I contribution in the O 1*s* spectrum. Moreover, it is also found a contribution at higher BE, 233.3 eV, which has been assigned to Mo^{6+} species in different chemical environments, denoted as Mo_{II} since it is related to the O_{II} contribution in the O 1*s* spectrum.[20] After the treatment with 5%H_2-Ar, there is a small reduction of Mo^{6+} to Mo^{5+}, as can be seen in Table S2, which includes the quantification of the corresponding Mo 3*d* and O 1*s* signals. This small increase in Mo^{5+} explains the minor change in cell parameters between as-prepared and reduced samples (Table S1). In addition, it is evidenced that $Gd_{5.4}Q$ contains the higher percentage of Mo^{5+}, both in the as-prepared and reduced samples, which might lead to a higher electronic conductivity in reducing conditions. Regarding Mo^{6+}, for $Sm_{5.4}Q$, the amount of Mo^{6+}(I) increases after reduction and, consequently, Mo^{6+}(II) decreases. The opposite behaviour after $Gd_{5.4}Q$ reduction is observed, i.e Mo^{6+}(I) decreases.

The Nd $3d_{5/2}$ spectrum shows an asymmetric peak at about 982.0 eV and weak broad shoulder from 972.0 to 980.0 eV, typical Nd 3*d* spectrum of Nd in different oxides (Figure S4).[37,38] The main component at 982.1 eV of the Nd $3d_{5/2}$ line is assigned to Nd^{3+} ions (here, in the oxide matrix) which remains after H_2 reduction. The low BE component is considered as the satellite of the main one (in the shake-down process). The BE separation between the main line component and its satellite, equal to -4.0 eV, lower than that found for Nd_2O_3, −4.5 eV and equal to that observed for $Nd_2Ti_2O_7$, -4.0 eV.[39] In our case, this should be due to the presence of neodymium molybdate.

The Sm core level spectra fit with that reported for Sm_2O_3 species, where the Sm $3d_{5/2}$ component is close to 1083.4 eV and the $3d_{3/2}$ one at 1110.0 eV.[40] Moreover, it is observed a shoulder in the Sm $3d_{5/2}$ component in the range of 1078.0 eV, due to the shake off satellite effect.[41] After H_2 treatment, the spectrum did not change.

Finally, the Gd $3d$-spectra also remained unchanged in both samples, and a profile typical of Gd_2O_3 oxide is observed,[42,43] with the $3d_{5/2}$ contribution located at 1187.0 eV and the Gd $3d_{3/2}$ one at 1220.0 eV, an energy difference of 33.0 eV.

3.5. Microstructural and electrical characterisation

SEM images of the pellet surfaces show that all the samples are fully dense after sintering at 1500 ºC with relative densities close to a 100% (Figure 6) and no secondary phases were observed. Moreover, EDS analysis confirms the homogeneous distribution of Nd, Sm, Gd and Mo, where no cation segregation was observed (Figure S5).

Particle size analysis shows that the average grain size of the samples decreases as the rare-earth radius becomes smaller (Figure S6), a tendency where lanthanum samples can be included,[20] presenting values of 15.8, 14.2, 11.5 and 5.5 μm for $La_{5.4}Q$, $Nd_{5.4}Q$, $Sm_{5.4}Q$ and $Gd_{5.4}Q$, respectively. A similar behaviour was reported by Amsif *et al.* for $BaCe_{0.9}Ln_{0.1}O_{3-\delta}$ (Ln = La, Nd, Sm, Gd and Yb),[44] where smaller lanthanides also led to a decrease of the average grain size of the ceramics and a reduction of the unit cell. In addition, it is observed a clear increase of the average grain size as the cooling rate decreases, i.e., 14.2, 18.3 and 20.0 μm for $Nd_{5.4}Q$, $Nd_{5.4}5$ and $Nd_{5.4}0.5$, respectively, due to the higher dwelling time at high sintering temperatures for the lower cooling rates (Figure S6). It must be highlighted that the anomaly observed between $La_{5.4}50$[20] and $Nd_{5.4}5$, with values of 16.2 and 18.3 μm, respectively, is caused by the different cooling rates. A cooling rate of 50ºC min^{-1} is very close to a sudden cooling, therefore the average grain size for $La_{5.4}50$ is nearer to that of $La_{5.4}Q$, 15.8 μm.[20]

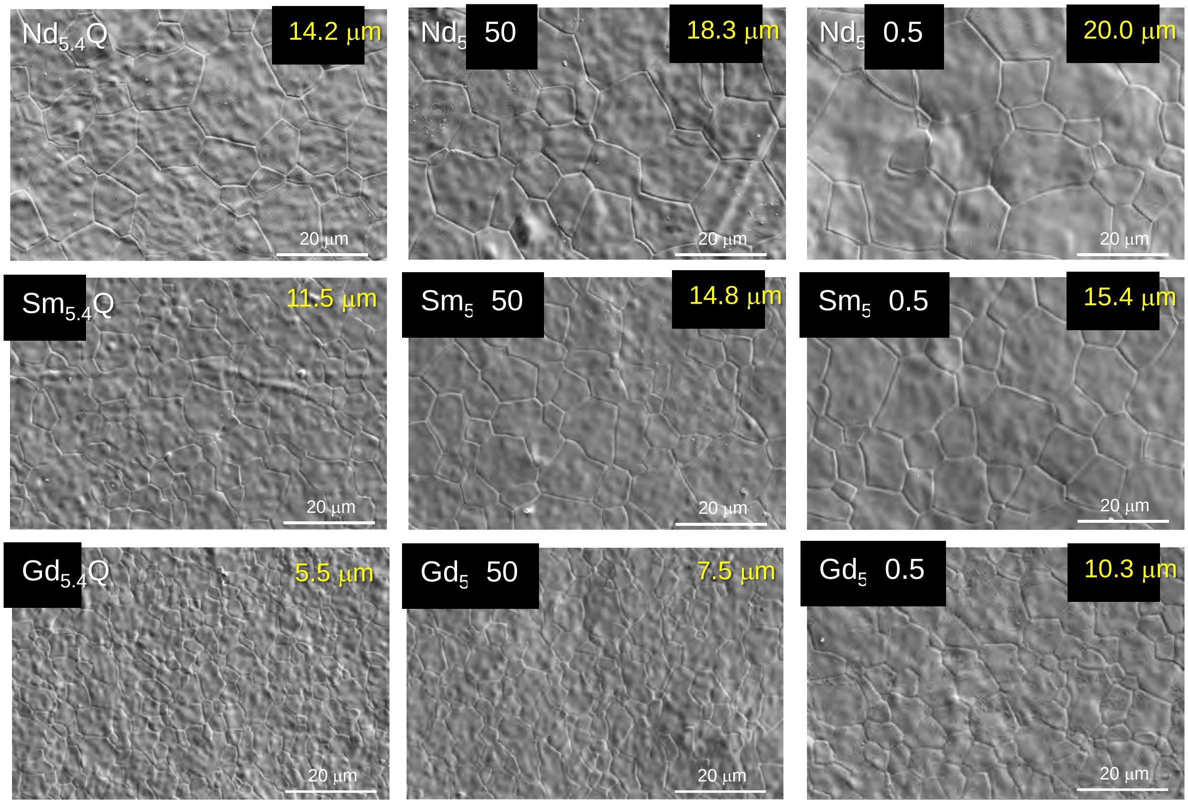

Figure 6. SEM micrographs of $Ln_{5.4}MoO_{11.1}$ (Ln = Nd, Sm and Gd) sintered at 1500 ºC for 1 h and cooled down at different rates. Average grain size is denoted at the top right of the images.

Impedance spectroscopy analysis of the samples, all sintered at 1500 ºC and cooled down by quenching, 5 or 0.5 ºC min^{-1}, was carried out under three different flowing atmospheres (dry/wet N_2 and wet 5% H_2−Ar) in order to determine the different contributions to the overall conductivity. Figure S7 shows the Nyquist plots at 400 ºC for $Ln_{5.4}Q$ (Ln = Nd, Sm and Gd) in dry and wet N_2. Only two contributions are detected in the spectra, assigned to the grain interior conduction (bulk) and the electrode process, with capacitances values in the order of pF cm^{-1} and mF cm^{-1}, respectively, which can be fitted with a $(R_bQ_b)(R_eQ_e)$ equivalent circuit model, where the subscripts *b* and *e* denote the grain interior and electrode processes, respectively. No grain boundary contribution to the overall conductivity is detected for any of the samples, regardless of the cooling rate, due to the large grain size of the samples without phase segregations at the grain boundary region. Shlyakhtina *et col.* reported a grain boundary contribution for related samples, such as $Sm_{5.5}MoO_{11.25}$[24] and Nd_6MoO_{12}[32] after several measurement cycles in dry and wet atmospheres (air and Ar). However, in this work, no grain boundary contributions are detected, even after several heating and cooling processes during the impedance spectroscopy analysis, suggesting a good cation homogeneity and stability of the samples.

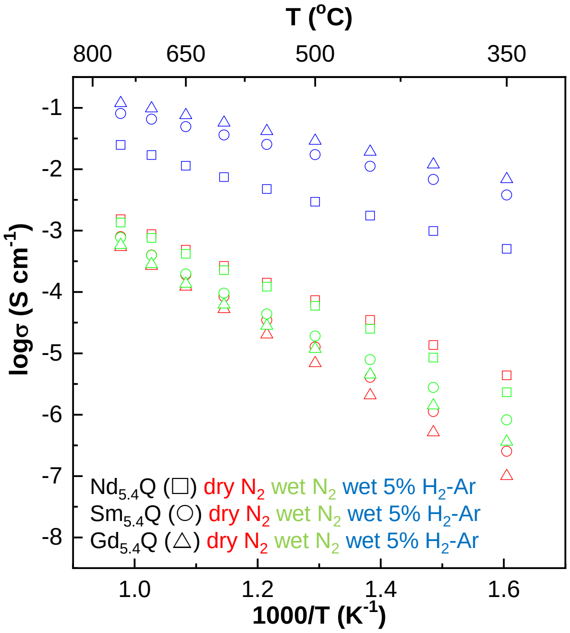

Figure 7. Arrhenius plots of $Ln_{5.4}MoO_{11.1}$ (Ln = Nd, Sm and Gd) sintered at 1500 ºC for 1 h and cooled down by quenching under dry and wet N_2 and wet 5%H_2-Ar atmospheres.

The Arrhenius plot shows for all Sm and Gd-containing samples, regardless of the cooling rate, a clear increase of the conductivity in a wet N_2 atmosphere respect to dry conditions (Figure 7 for the quenched samples and Table 2 for all compositions), due to a significant proton contribution to the conductivity, more prominent at temperatures lower than 650 ºC. The same behaviour was already reported for $La_{5.4}MoO_{11.1}$.[20] In addition, the differences between the conductivity in dry and wet conditions is more important for samples with higher lanthanide size, La>Sm>Gd, meaning that the proton conductivity decreases for smaller cations. However, this is not detected for Nd-samples, where the conductivity values are lower in wet conditions than in dry conditions. This behaviour may be ascribed to the presence of a significant p-type electronic contribution to the overall conductivity under oxidizing conditions as described below.

A clear relationship between the lanthanide type, cooling conditions and conductivity can be established from Table 2 and Figure 7. The samples prepared in this work present higher conductivity values than the analogous La-containing compounds,[20] with values of 0.17, 0.87, 0.4 and 0.26 mS cm^{-1}, for $La_{5.4}Q$, $Nd_{5.4}Q$, $Sm_{5.4}Q$ and $Gd_{5.4}Q$, respectively, at 700 ºC in a dry N_2 atmosphere. This higher conductivity respect to $La_{5.4}Q$ may be ascribed to a more significant p-type electronic contribution to the conductivity for the Nd sample that decreases for Sm and Gd. Moreover, this drop in conductivity can also be related to a lower ionic conductivity due to the decrease of the cell volumes (Table 1) along the lanthanide series, hindering the ion mobility. On the other hand, within the same lanthanide element, the highest conductivity is always observed for the quenched samples, due to their higher symmetry (Table 2). Activation energies clearly increases as the lanthanide size decreases, with values of 0.80(1), 1.10(1) and 1.17(1) eV for $Nd_{5.4}Q$, $Sm_{5.4}Q$ and $Gd_{5.4}Q$, respectively, in dry N_2, indicating an increasing constriction in the conduction mechanism from Nd to Gd as the lattice cell volume decreases. In a wet N_2 atmosphere, the activation energies in the low temperature (LT) region are smaller than those at high temperature (HT), due to the proton contribution to the overall conductivity. For instance, $Sm_{5.4}Q$ presents a value of 0.87(1) eV at LT and of 1.07(1) eV at HT. The remaining compositions exhibit a similar behaviour.

In a very reducing atmosphere, 5% H_2-Ar, a significant enhancement of the conductivity due to a n-type electronic contribution can be observed (Figure 7 and Table 2), which is caused by the reduction of Mo^{6+} to Mo^{5+}, as XPS studies showed (Table S2), according to:

$$2\mathrm{Mo}_{\mathrm{Mo}}^{\mathrm{x}} + \mathrm{O}_{\mathrm{O}}^{\mathrm{x}} \rightarrow 2\mathrm{Mo}_{\mathrm{Mo}}' + \mathrm{V}_{\mathrm{O}}^{\cdot\cdot} + 1/2\ \mathrm{O}_2 \qquad (1)$$

The conductivity clearly increases as the lanthanide size becomes smaller, with values of 5.0, 17.0, 65.1 and 98.0 mS cm^{-1}, for $La_{5.4}Q$, $Nd_{5.4}Q$, $Sm_{5.4}Q$ and $Gd_{5.4}Q$, respectively, at 700 ºC in a wet 5% H_2-Ar atmosphere. This is clearly due to the decrease in cell volumes from lanthanum to gadolinium samples, making the molybdenum atoms closer to each other, facilitating the electron transfer, and the increase in Mo^{5+} concentration on reduction (Table S2). This behaviour is also reflected in the activation energies, with values of 0.72(1), 0.52(1), 0.43(1) and 0.40(1) eV for $La_{5.4}Q$[20], $Nd_{5.4}Q$, $Sm_{5.4}Q$ and $Gd_{5.4}Q$, respectively. A similar behaviour is reported for the remaining samples.

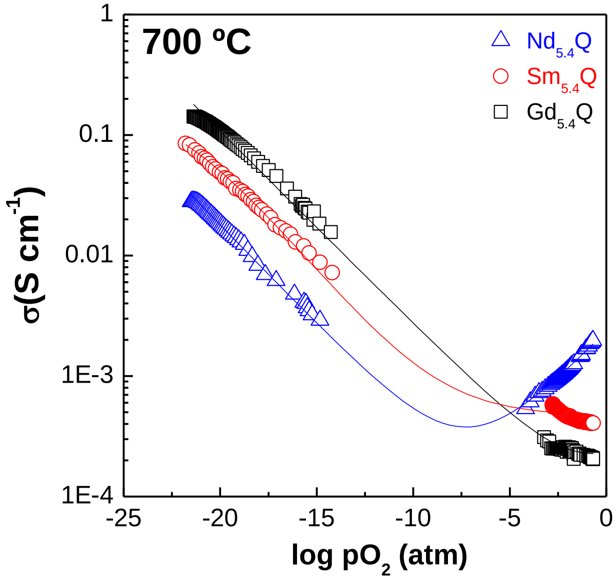

Figure 8. Dependence of the overall conductivity as a function of the oxygen partial pressure at 700 °C for $Nd_{5.4}Q$, $Sm_{5.4}Q$ and $Gd_{5.4}Q$. The solid line is the fitting with Eq 2.

The variation of the conductivity with the oxygen partial pressure confirms that all materials are mixed ionic-electronic conductor with a predominant n-type electronic contribution under reducing conditions (Figure 8). The increase of electronic conductivity at high pO_2 values is attributed to a p-type electronic contribution, which is more significant for $Nd_{5.4}Q$. The curves were adequately fitted by the following equation previously used for related lanthanum molybdates:[20]

$$\sigma = \sigma_i + \sigma_n pO_2^{-1/6} + \sigma_p pO_2^{1/6} \qquad (2)$$

where σ_i is the ionic conductivity, and σ_n and σ_p are the n-type and p-type electronic conductivity, respectively. This curve clearly indicated that the n-type electronic conductivity increases with decreasing the ionic radii of the RE cation in the order Gd > Sm > Nd. In contrast, the ionic conductivity follows the opposite trend, associated to the decrease in the cell volumes. The p-type contribution does not follow a clear relationship between conductivity and ionic radii.

CONCLUSIONS

$Ln_{5.4}MoO_{11.1}$ (Ln = Nd, Sm and Gd) compositions were prepared by the freeze-drying precursor method. XRPD analysis revealed that the final symmetry of the samples depends on the size of the lanthanide cation and the cooling rate. Samples suddenly cooled from 1500 ºC exhibit a cubic fluorite symmetry, where Ln and Mo are completely disordered at high temperature, stabilising the kinetically more stable cubic phase. At slower cooling rates, thermodynamically stable phases start to prevail and the lanthanide size plays a key role. In the case of larger lanthanides and slower cooling rates, the R1 symmetry is the more stable form. Conversely, for smaller lanthanides and faster cooling rates, the cubic symmetry is preferred due to a less pronounced size mismatch between cations. However, SAED and HR-TEM studies reveal that the symmetry of the non-quenched samples cannot be univocally described with XRPD analysis, where crystalline domains with different symmetries coexist.

XPS analysis reveals that all samples present a significant amount of Mo^{5+}, which slightly increases on very reducing conditions, where all the compositions are stable. Impedance spectroscopy analysis in a N_2 atmosphere show a decrease of the ionic conductivity as the lanthanide size becomes smaller due to a hindering of the conduction pathways caused by the shrinking of the framework. On the other hand, in a very reducing 5% H_2-Ar atmosphere, the electronic conductivity increases for the smaller lanthanides due to larger amount of Mo^{5+} on reduction and the increased proximity of the Mo centres caused by the smaller unit cell.

AUTHOR INFORMATION

Corresponding Author

e-mail address: josema@uma.es (José Manuel Porras Vázquez)

Present address: Dpto. de Química Inorgánica, Cristalografía y Mineralogía, Facultad de Ciencias, Campus de Teatinos, Universidad de Málaga, 29071-Málaga, Spain.

Tel: +34 952131877

AUTHOR CONTRIBUTIONS

Conceptualization: J.M.P-V. and E.R.L; methodology: J.M.P-V., D.M-L. and E.R.L.; investigation: R.R-V., J.M.P-V., L.d.S.-G., J.Z.-G., A.I-M., and J.C-V.; formal analysis: J.M.P.-V., A.I-M., J.C-V, and D.M.-L.; validation: J.M.P.-V, D.M.-L. and E.R.L.; visualization: R.R-V., J.M.P-V. and D.M.-L.; project administration: J.M.P-V., D.M-L. and E.R.L.; writing—original draft: R.R-V and J.M.P-V.; writing—review and editing: J.M.P.-V., E.R.L. and D.M.-L.

CONFLICTS OF INTEREST

There are no conflicts to declare.

ACKNOWLEDGEMENTS

This work was supported by *Ministerio de Ciencia e Innovación* through the PID2021-126009OB-I00 and PID2019-110249RB-I00 research projects and *Junta de Andalucía* through UMA18-FEDERJA-033 research grants (Spain). JCV thanks UCLM (*Ayuda a Grupos Plan Propio*) and JCCM-FEDER for funding through grant 2020-GRIN-29130. JZG thanks the *Ministerio de Universidades* for his FPU17/02621 grant.

REFERENCES

[1] A. Midilli, M. Ay, I. Dincer, M.A. Rosen, On hydrogen and hydrogen energy strategies II: future projections affecting global stability and unrest, Renewable Sustainable Energy Rev. 9 (2005) 273−287.

[2] C.J. Winter, Hydrogen energy-Abundant, efficient, clean: a debate over the energy-system-of-change, Int. J. Hydrogen Energy 34 (2009) S1−S52.

[3] M. Momirlan, T.N. Veziroglu, The properties of hydrogen as fuel tomorrow in sustainable energy system for a cleaner planet, Int. J. Hydrogen Energy 30 (2005) 795−802.

[4] A. Kudo, Y. Miseki, Heterogeneous photocatalyst materials for water splitting, Chem. Soc. Rev. 8 (2009) 253−278.

[5] M.G. Walter, E.L. Warren, J.R. McKone, S.W. Boettcher, Q.X. Mi, E.A. Santori, N.S. Lewis, Solar Water Splitting Cells, Chem. Rev. 110 (2010) 6446−6473.

[6] R.D. Cortright, R.R. Davda, J.A. Dumesic, Hydrogen from catalytic reforming of biomass-derived hydrocarbons in liquid water, Nature 418 (2002) 964−967.

[7] S. Ahmed, M. Krumpelt, Hydrogen from hydrocarbon fuels for fuel cells, 26 (2001) 291−301.

[8] Z. Tao, L. Yan, J. Qiao, B. Wanga, L. Zhang, J. Zhang, A review of advanced proton-conducting materials for hydrogen separation, Prog. Mater. Sci. 74 (2015) 1–50.

[9] N.W. Ockwig, T.M. Nenoff, Membranes for Hydrogen Separation, Chem. Rev. 107 (2007) 4078–4110.

[10] K.H. Ryu, S.M. Haile, Chemical stability and proton conductivity of doped $BaCeO_3$-$BaZrO_3$ solid solutions, Solid State Ion. 125 (1999) 355–367.

[11] H. Iwahara, H. Uchida, K. Ono, K. Ogaki, Proton conduction in sintered oxides based on $BaCeO_3$, J. Electrochem. Soc. 135 (1988) 529–533.

[12] K.H. Ryu, S.M. Haile, Chemical stability and proton conductivity of doped $BaCeO_3$-$BaZrO_3$ solid solutions, Solid State Ion. 125 (1999) 355−367.

[13] N. Zakowsky, S. Williamson, J.T.S. Irvine, Elaboration of CO_2 tolerance limits of $BaCe_{0.9}Y_{0.1}O_{3-\delta}$ electrolytes for fuel cells and other applications, Solid State Ion. 176 (2005) 3019−3026.

[14] A. Magrasó, C. Frontera, D. Marrero-López, P. Nuñez, New crystal structure and characterization of lanthanum tungstate “La_6WO_{12}” prepared by freeze-drying synthesis, Dalton Trans. 2009, 10273–10283.

[15] C. Solís, S. Escolástico, R. Haugsrud, J.M. Serra, $La_{5.5}WO_{12-\delta}$ Characterization of Transport Properties under Oxidizing Conditions: A Conductivity Relaxation Study, J. Phys. Chem. C 115 (2011) 11124–11131.

[16] J.M. Porras-Vázquez, L. dos Santos-Gómez, D. Marrero-López, P.R. Slater, N. Masó, A. Magrasó, E.R. Losilla, Effect of tri- and tetravalent metal doping on the electrochemical properties of lanthanum tungstate proton conductors, Dalton Trans. 45 (2016), 3130–3138.

[17] M. Amsif, A. Magrasó, D. Marrero-López, J.C. Ruiz-Morales, J. Canales-Vázquez, P. Núñez, Mo-Substituted Lanthanum Tungstate $La_{28-y}W_{4+y}O_{54+\delta}$: A Competitive Mixed Electron−Proton Conductor for Gas Separation Membrane Applications, Chem. Mater. 24 (2012) 3868−3877.

[18] Y. Chen, Q. Liao, Z. Li, H. Wang, Y. Wei, A. Feldhoff, J. Caro, A CO_2-Stable Hollow-Fiber Membrane with High Hydrogen Permeation Flux, AIChE 61 (2015) 1997−2007.

[19] S. Escolástico, S. Somacescu, J.M. Serra, Tailoring mixed ionic–electronic conduction in H_2 permeable membranes based on the system $Nd_{5.5}W_{1-x}Mo_xO_{11.25-\delta}$, J. Mater. Chem. A 3 (2015) 719-731.

[20] A. López-Vergara, J.M. Porras-Vázquez, A. Infantes-Molina, J. Canales-Vázquez, A. Cabeza, E.R. Losilla, D. Marrero-López, Effect of Preparation Conditions on the Polymorphism and Transport Properties of $La_{6-x}MoO_{12-\delta}$ $(0 \leq x \leq 0.8)$, Chem. Mater. 29 (2017) 6966−6975.

[21] A. López-Vergara, L. Vizcaíno-Anaya, J.M. Porras-Vázquez, G. Baldinozzi, L. dos Santos-Gómez, J. Canales-Vazquez, D. Marrero-López, E.R. Losilla, Unravelling Crystal Superstructures and Transformations in the $La_{6-x}MoO_{12-\delta}$ ($0.6 \leq x \leq 3.0$) Series: A System with Tailored Ionic/Electronic Conductivity, Chem. Mater. 32 (2020) 7052−7062.

[22] T. Dan Vu, F. Krichen, M. Barré, S. Coste, A. Jouanneaux, E. Suard, A. Fitch, F. Goutenoire, Ab-initio structure determination of $La_{34}Mo_8O_{75}$ using powder X-ray and neutron diffraction data, Cryst. Growth Des. 19 (2019) 6074−6081.

[23] P.M. de Wolff, Symmetry operations for displacively modulated structures, Acta Crystallogr., Sect. A: Cryst. Phys., Diffr., Theor. Gen. Crystallogr. 33 (1977) 493−497.

[24] A.V. Shlyakhtina, S.N. Savvin, N.V. Lyskov, I. V. Kolbanev, O. K. Karyagina, S. A. Chernyak, L. G. Shcherbakova, P. Núñez, Polymorphism in the family of $Ln_{6-x}MoO_{12-\delta}$ (Ln = La, Gd–Lu; $x = 0, 0.5$) oxygen ion- and proton-conducting materials, J. Mater. Chem. A, 5 (2017) 7618–7630.

[25] A.V. Shlyakhtina, S.N. Savvin, N.V. Lyskov, D.A. Belov, A.N. Shchegolikhin, I.V. Kolbanev, O.K. Karyagina, S.A. Chernyak, L.G. Shcherbakova, P. Núñez, $Sm_{6-x}MoO_{12-\delta}$ ($x = 0, 0.5$) and Sm_6WO_{12} – Mixed electron-proton conducting materials, Solid State Ion. 302 (2017) 143–151.

[26] X'Pert High Score Plus Program, version 3.0e; PANalytical B.V.: Amelo, The Netherlands, 2012.

[27] A. C. Larson, R. B. von Dreele, GSAS Program; Report LA-UR-86748; Los Alamos National Lab, 1994.

[28] Digital Micrograph, version 3.22.1461.0; Gatan: Pleasanton, CA.

[29] J. C. C. Abrantes, Estereologiá, UIDM, ESTG; Polytechnic Institute of Viana do Castelo: Viana do Castelo, Portugal, 1998.

[30] D. Johnson, ZView: A Software Program for IES Analysis, versión 2.9c; Scribner Associates, Inc.: Southern Pines, NC, 2005.

[31] A. López-Vergara, J.M. Porras-Vázquez, E. Vøllestad, J. Canales-Vázquez, E.R. Losilla, D. Marrero-López, Metal-Doping of $La_{5.4}MoO_{11.1}$ Proton Conductors: Impact on the Structure and Electrical Properties, Inorg. Chem. 57 (2018) 12811−12819.

[32] S.N. Savvin, M. Avdeev, I.V. Kolbanev, E.P. Kharitonova, L.G. Shcherbakova, A.V. Shlyakhtina, P. Nuñez, Stability against reduction of fluorite-like rhombohedral $La_{5.5}MoO_{11.25}$ and $Ho_{5.4}Zr_{0.6}MoO_{12.3}$ fluorite: Conductivity and neutron diffraction study, Solid State Ion. 319 (2018) 148–155.

[33] A. V. Shlyakhtina, M. Avdeev, J. C. C. Abrantes, E. Gomes, N. V. Lyskov, E. P. Kharitonova, I. V. Kolbanev, L.G. Shcherbakova, Structure and conductivity of Nd_6MoO_{12}-based potential electron–proton conductors under dry and wet redox conditions, Inorg. Chem. Front. 6 (2019) 566–575.

[34] S.N. Savvin, A.V. Shlyakhtina, A.B. Borunova, L.G. Shcherbakova, J.C. Ruiz-Morales, P. Núñez, Crystal structure and proton conductivity of some Zr-doped rare-earth molybdates, Solid State Ion. 271 (2015) 91–97.

[35] J. Zamudio-García, J.M. Porras-Vázquez, J. Canales-Vázquez, A. Cabeza, E.R. Losilla, D. Marrero-López, Relationship between the Structure and Transport Properties in the $Ce_{1-x}La_xO_{2-x/2}$ System, Inor. Chem. 58 (2019) 9368−9377.

[36] NIST Standard Reference Database 20, Version 4.1, 2012.

[37] Y.A. Teterin, A.Y. Teterin, Structure of X-ray photoelectron spectra of lanthanide compounds, Russ. Chem. Rev. 71 (2002) 347–381.

[38] V.V. Atuchin, T.A. Gavrilova, J.C. Grivel, V.G. Kesler, Electronic structure of layered titanate $Nd_2Ti_2O_7$, Surf. Sci. 602 (2008) 3095–3099.

[39] R.J. Iwanowski, M.H. Heinonen, I. Pracka, J. Kachniarz, XPS characterization of single crystalline $SrLaGa_3O_7$:Nd, Appl. Surf. Sci. 283 (2013) 168–174.

[40] H. Brunckova, M. Kanuchova, H. Kolev, E. Mudra, L. Medvecky, XPS characterization of $SmNbO_4$ and $SmTaO_4$ precursors prepared by sol-gel method, Appl. Surf. Sci. 473 (2019) 1–5.

[41] Y. Kim, H. Schlegl, K. Kim, J.T.S. Irvine, J.H. Kim, X-ray photoelectron spectroscopy of Sm-doped layered perovskite for intermediate temperature-operating solid oxide fuel cell, Appl. Surf. Sci. 288 (2014) 695–701.

[42] C.V. Prasad, M.S.P. Reddy, V.R. Reddy, C. Park, Effect of annealing on chemical, structural and electrical properties of Au/Gd_2O_3/n-GaN heterostructure with a high-k rare-earth oxide interlayer, Appl. Surf. Sci. 427 (2018) 670–677.

[43] H. Brunckova, H. Kolev, L.A. Rocha, E.J. Nassar, S.B. Moscardini, L. Medvecky, XPS characterization and luminescent properties of $GdNbO_4$ and $GdTaO_4$ thin films, Appl. Surf. Sci. 504 (2020) 144358.

[44] M. Amsif, D. Marrero-Lopez, J.C. Ruiz-Morales, S.N. Savvin, M. Gabás, P. Nunez, Influence of rare-earth doping on the microstructure and conductivity of $BaCe_{0.9}Ln_{0.1}O_{3-\delta}$ proton conductors, J. Power Sources 196 (2011) 3461–3469.

Tables

Table 1. Polymorphic phases, unit cell parameters and agreement factors for $Ln_{5.4}MoO_{11.1}$ (Ln = Nd, Sm and Gd) sintered at 1500 ºC and cooled down at different rates (quenching, 5 and 0.5 ºC min^{-1}).

	Cooling rate	**Symmetry**	**a (Å)**	**c (Å)**	**V/Z (Å^3)**	**R_{wp} (%)**	**R_F (%)**
$Nd_{5.4}MoO_{11.1}$	Quenching	Cubic	5.5231(1)	-	42.12(1)	3.44	2.85
	5 ºC min^{-1}	R1	3.8864(1)	9.6604(1)	42.12(1)	4.55	3.07
	0.5 ºC min^{-1}	R1	3.8868(1)	9.6629(1)	42.14(1)	3.99	2.80
$Sm_{5.4}MoO_{11.1}$	Quenching	Cubic	5.4421(1)	-	40.29(1)	2.65	2.59
	5 ºC min^{-1}	Cubic	5.4434(1)	-	40.32(1)	2.26	2.35
	0.5 ºC min^{-1}	R1	3.8244(1)	9.5335(1)	40.34(1)	2.35	2.58
$Gd_{5.4}MoO_{11.1}$	Quenching	Cubic	5.3921(1)	-	39.19(1)	1.93	2.35
	5 ºC min^{-1}	Cubic	5.3877(1)	-	39.10(1)	2.21	2.25
	0.5 ºC min^{-1}	Cubic	5.3693(1)	-	38.58(1)	2.37	1.95

Table 2. Conductivity values at 700 and 400 ºC for $Ln_{5.4}MoO_{11.1}$ (Ln = Nd, Sm and Gd) cooled down at different rates (quenching, 5 and 0.5 ºC min^{-1}) under dry and wet N_2 and wet 5% H_2-Ar atmospheres.

Sample	**Average grain size (μm)**	**dry N_2**		**wet N_2**		**wet 5% H_2-Ar**	
		σ_{700} (mS cm^{-1})	**σ_{400} (mS cm^{-1})**	**σ_{700} (mS cm^{-1})**	**σ_{400} (mS cm^{-1})**	**σ_{700} (mS cm^{-1})**	**σ_{400} (mS cm^{-1})**
$La_{5.4}Q$[20]	15.8	$1.7\ 10^{-1}$	$2.3\ 10^{-3}$	$2.5\ 10^{-1}$	$1.1\ 10^{-2}$	5.0	$2.0\cdot10^{-1}$
$La_{5.4}50$[20]	16.2	$7.2\ 10^{-2}$	$1.7\ 10^{-3}$	$1.4\ 10^{-1}$	$7.4\ 10^{-3}$	4.0	$2.6\ 10^{-1}$-
$La_{5.4}0.5$[20]	21.2	$9.0\ 10^{-2}$	$1.7\ 10^{-3}$	$1.9\ 10^{-1}$	$1.9\ 10^{-2}$	$4.5\ 10^{-1}$	$2.3\ 10^{-2}$
$Nd_{5.4}Q$	14.2	$8.7\ 10^{-1}$	$1.4\ 10^{-2}$	$7.5\ 10^{-1}$	$8.5\ 10^{-3}$	17.0	1.0
$Nd_{5.4}5$	18.3	$3.9\ 10^{-1}$	$5.3\ 10^{-3}$	$3.7\ 10^{-1}$	$4.0\ 10^{-3}$	16.8	1.1
$Nd_{5.4}0.5$	20.0	$2.7\ 10^{-1}$	$3.7\ 10^{-3}$	$2.4\ 10^{-1}$	$2.8\ 10^{-3}$	17.3	1.2
$Sm_{5.4}Q$	11.5	$4.0\ 10^{-1}$	$1.1\ 10^{-3}$	$3.9\ 10^{-1}$	$2.8\ 10^{-3}$	65.1	6.8
$Sm_{5.4}5$	14.8	$3.5\ 10^{-1}$	$9.9\ 10^{-4}$	$3.6\ 10^{-1}$	$2.9\ 10^{-3}$	50.5	5.0
$Sm_{5.4}0.5$	15.4	$4.0\ 10^{-1}$	$1.1\ 10^{-3}$	$4.3\ 10^{-1}$	$2.7\ 10^{-3}$	52.7	4.3
$Gd_{5.4}Q$	5.5	$2.6\ 10^{-1}$	$5.1\ 10^{-4}$	$2.8\ 10^{-1}$	$1.4\ 10^{-3}$	98.0	11.9
$Gd_{5.4}5$	7.5	$1.7\ 10^{-1}$	$6.3\ 10^{-5}$	$2.0\ 10^{-1}$	$7.2\ 10^{-4}$	83.9	13.7
$Gd_{5.4}0.5$	10.3	$4.1\ 10^{-2}$	$4.5\ 10^{-5}$	$9.7\ 10^{-2}$	$4.2\ 10^{-4}$	92.8	22.2

Table S1. Polymorphic phases, unit cell parameters and agreement factors for $Ln_{5.4}MoO_{11.1}$ (Ln = Nd, Sm and Gd) sintered at 1500 ºC, cooled down at different rates (quenching, 5 and 0.5 ºC min^{-1}) after annealing at 800 ºC for 24 h in a 5%H_2-Ar atmosphere.

	Cooling rate	**Symmetry**	**a (Å)**	**c (Å)**	**V/Z (Å^3)**	**R_{wp} (%)**	**R_F (%)**
$Nd_{5.4}MoO_{11.1}$	Quenching	Cubic	5.5223(1)	-	42.10(1)	8.55	3.04
	5 ºC min^{-1}	R1	3.8868(2)	9.6582(6)	42.12(1)	8.89	-
	0.5 ºC min^{-1}	R1	3.8886(1)	9.6663(4)	42.19(1)	8.69	-
$Sm_{5.4}MoO_{11.1}$	Quenching	Cubic	5.4370(1)	-	40.18(1)	7.16	3.91
	5 ºC min^{-1}	Cubic	5.4356(1)	-	40.15(1)	6.86	3.59
	0.5 ºC min^{-1}	R1	3.8307(3)	9.5366(1)	40.40(1)	7.62	-
$Gd_{5.4}MoO_{11.1}$	Quenching	Cubic	5.3822(1)	-	38.98(1)	6.10	3.15
	5 ºC min^{-1}	Cubic	5.3804(1)	-	38.94(1)	6.54	3.99
	0.5 ºC min^{-1}	Cubic	5.3659(1)	-	38.62(1)	5.85	2.08

Table S2. Atomic percentage of Mo^{5+}, Mo^{6+} and O^{2-} in their different coordination environments obtained from the analysis of the XPS spectra.

	Nd$_{5.4}$Q		**Sm$_{5.4}$Q**		**Gd$_{5.4}$Q**	
	As-prepared	Reduced	As-prepared	Reduced	As-prepared	Reduced
Mo^{5+}	-	-	5.6	7.2	8.9	9.9
Mo^{6+} (I)	-	-	75.2	79.3	70.7	65.5
Mo^{6+} (II)	-	-	19.2	13.6	20.4	24.6
O$_{I}$	52.4	74.7	53.3	62.5	48.3	40.7
O$_{II}$	23.4	25.3	33.3	34.1	32.3	38.3
O$_{III}$	24.2	-	13.4	3.5	19.4	21.1